

See discussions, stats, and author profiles for this publication at: <https://www.researchgate.net/publication/231238830>

# Self-Assembly of Photofunctional Cylindrical Nanostructures Based on Perylene-3,4:9,10-bis(dicarboximide)

ARTICLE *in* CHEMISTRY OF MATERIALS · NOVEMBER 2005

Impact Factor: 8.35 · DOI: 10.1021/cm051461s

CITATIONS

81

READS

29

9 AUTHORS, INCLUDING:



**Louise E Sinks**

US Nano LLC

31 PUBLICATIONS 1,826 CITATIONS

SEE PROFILE



**Xiaobing Zuo**

Argonne National Laboratory

96 PUBLICATIONS 2,078 CITATIONS

SEE PROFILE



**David M. Tiede**

Argonne National Laboratory

165 PUBLICATIONS 6,275 CITATIONS

SEE PROFILE



**Xiyu Li**

Shandong University

76 PUBLICATIONS 1,930 CITATIONS

SEE PROFILE

# Self-Assembly of Photofunctional Cylindrical Nanostructures Based on Perylene-3,4,9,10-bis(dicarboximide)

Louise E. Sinks,<sup>†</sup> Boris Rybtchinski,<sup>†</sup> Masanori Iimura,<sup>†</sup> Brooks A. Jones,<sup>†</sup>  
Andrew J. Goshe,<sup>‡</sup> Xiaobing Zuo,<sup>‡</sup> David M. Tiede,<sup>‡</sup> Xiyu Li,<sup>\*,†</sup> and  
Michael R. Wasielewski<sup>\*,†</sup>

Department of Chemistry and Center for Nanofabrication and Molecular Self-Assembly, Northwestern University, Evanston, Illinois 60208-3113, and Chemistry Division, Argonne National Laboratory, Argonne, Illinois 60439

Received July 6, 2005. Revised Manuscript Received October 19, 2005

A perylene-3,4,9,10-bis(dicarboximide)-based electron donor–acceptor monomer was designed to self-assemble using the synergistic effects of  $\pi$ – $\pi$  stacking, microsegregation, and hydrogen bonding. The resulting aggregates were characterized in solution by small-angle X-ray scattering (SAXS), while the solid-state structure was probed by X-ray diffraction, transmission electron microscopy, and scanning electron microscopy. The solution-phase assemblies were found to consist of 12 monomers arranged in either a face-to-face stacked pair of hydrogen-bonded hexagonal arrays or a two-turn helix. The SAXS data do not allow a clear distinction between these two cyclic motifs. These cyclic arrays grow to lengths of about 1  $\mu$ m and form bundles of cylindrical structures in the solid phase. Aggregation is solvent dependent, with methylcyclohexane inducing aggregation and tetrahydrofuran disrupting it. The solution-phase photophysics of the dodecamer were probed by UV–vis, time-resolved fluorescence, and femtosecond transient absorption spectroscopies, revealing that formation of the dodecamer introduces an ultrafast electron-transfer pathway that is not present in the monomer.

## Introduction

The efficient control over energy and electron transfer found in photosynthetic light-harvesting and reaction center proteins is a consequence of the well-ordered assemblies of photofunctional chromophores within them.<sup>1–6</sup> The synthesis of bioinspired photofunctional arrays of chromophores having ordered structures is proving important in the design and development of advanced organic materials for electronics and photonics.<sup>7–9</sup> Synthesizing large covalent structures requires great effort, while using noncovalent interactions to self-assemble small molecules into large supramolecular structures is more appealing for the design of functional materials. Several research groups have attempted to correlate the nature of weak associative noncovalent interactions with resultant supramolecular structures, and many of the most successful design strategies rely on a variety of complementary associative interactions. Examples of such hierarchical

self-organization include the work of Würthner et al., which utilizes hydrogen-bonding, microsegregation, and  $\pi$ – $\pi$  interactions to create tapes and helices of perylenediimides (PDIs),<sup>10–13</sup> and that of Meijer and co-workers, which uses similar interactions to assemble oligo(*p*-phenylenevinylene)s into cylinders and tubes.<sup>14–16</sup>

The effort to create functional supramolecular structures has focused on the preservation of functionality built into the component units. For example, numerous supramolecular structures based on PDIs have emphasized the retention of their high fluorescence quantum yields.<sup>10–12,17</sup> Other researchers have introduced chiral substituents, in an effort to template chirality in the assembly.<sup>16,18,19</sup> Several research groups have created functional supramolecular structures from mixtures of components, which combine to create

\* To whom correspondence should be addressed. E-mail: wasielew@chem.northwestern.edu.

<sup>†</sup> Northwestern University.

<sup>‡</sup> Argonne National Laboratory.

- (1) Walz, T.; Jamieson, S. J.; Bowers, C. M.; Bullough, P. A.; Hunter, C. N. *J. Mol. Biol.* **1998**, *282*, 833–845.
- (2) Savage, H.; Cyrklaff, M.; Montoya, G.; Kuhlbrandt, W.; Sinning, I. *Structure* **1996**, *4*, 243–252.
- (3) Huber, R. *Angew. Chem., Int. Ed. Engl.* **1989**, *28*, 848–869.
- (4) Pullerits, T.; Sundström, V. *Acc. Chem. Res.* **1996**, *29*, 381–389.
- (5) McLuskey, K.; Prince, S. M.; Cogdell, R. J.; Isaacs, N. W. *Biochemistry* **2001**, *40*, 8783–8878.
- (6) McDermott, G.; Prince, S. M.; Freer, A. A.; Hawthornthwaite-Lawless, A. M.; Papiz, M. Z.; Cogdell, R. J.; Isaacs, N. W. *Nature* **1995**, *374*, 517–521.
- (7) Reinhoudt, D. N.; Crego-Calama, M. *Science* **2002**, *295*, 2403–2407.
- (8) Lehn, J.-M. *Science* **2002**, *295*, 2400–2403.
- (9) Ikkala, O.; ten Brinke, G. *Science* **2002**, *295*, 2407–2409.

- (10) Würthner, F.; Thalacker, C.; Sautter, A. *Adv. Mater.* **1999**, *11*, 754–758.
- (11) Thalacker, C.; Würthner, F. *Adv. Funct. Mater.* **2002**, *12*, 209–218.
- (12) Würthner, F.; Thalacker, C.; Sautter, A.; Scharlt, W.; Ibach, W.; Hollricher, O. *Chem.—Eur. J.* **2000**, *6*, 3871–3886.
- (13) Sautter, A.; Thalacker, C.; Würthner, F. *Angew. Chem., Int. Ed.* **2001**, *40*, 4425–4428.
- (14) Schenning, A. P. H. J.; Jonkheijm, P.; Peeters, E.; Meijer, E. W. *J. Am. Chem. Soc.* **2001**, *123*, 409–416.
- (15) Jonkheijm, P.; Miura, A.; Zdanowska, M.; Hoebe, F. J. M.; Feyter, S. D.; Schenning, A. P. H. J.; Schryver, F. C. D.; Meijer, E. W. *Angew. Chem., Int. Ed.* **2004**, *43*, 74–78.
- (16) Gesquiere, A.; Jonkheijm, P.; Hoebe, F. J. M.; Schenning, A. P. H. J.; De Feyter, S.; De Schryver, F. C.; Meijer, E. W. *Nano Lett.* **2004**, *4*, 1175–1179.
- (17) Sui, G.; Orbulescu, J.; Mabrouki, M.; Leblanc, R. M.; Liu, S.; Gregg, B. A. *ChemPhysChem* **2002**, *3*, 1041–1044.
- (18) Claussen, R. C.; Rabatic, B. M.; Stupp, S. I. *J. Am. Chem. Soc.* **2003**, *125*, 12680–12681.
- (19) Fenniri, H.; Deng, B.-L.; Ribbe, A. E. *J. Am. Chem. Soc.* **2002**, *124*, 11064–11072.

functionality that is not present in the constituent parts. The most common motif for such functional structures is a mixture of electron-donor and electron-acceptor components, whose self-assembly results in a supramolecular structure that undergoes photoinduced electron transfer. Examples include hexabenzocoronene liquid crystal/PDI,<sup>20</sup> zinc phthalocyanine/liquid crystalline PDI,<sup>21</sup> and oligo(*p*-phenylenevinylene)/PDI<sup>22</sup> mixtures. We report here the preparation, structure, and photophysical properties of self-assembled cylindrical nanostructures that demonstrate photoinduced electron transfer arising from a single asymmetric covalent module based on PDI. The electron-transfer events are controlled by the noncovalent interactions that introduce new efficient electron-transfer pathways.

## Experimental Section

**Optical Spectroscopy.** Steady-state absorption and emission spectra were obtained on a Shimadzu 1601 UV–vis spectrophotometer and a PTI single-photon-counting spectrofluorimeter in a right angle configuration, respectively. A 10 or 2 mm path length quartz cuvette was used for the absorption measurements as indicated, while a 10 mm quartz cuvette was used for the fluorescence measurements. The optical density at  $\lambda_{\text{max}}$  for the fluorescence measurements was maintained at  $0.1 \pm 0.05$  to avoid reabsorption artifacts.

Femtosecond transient absorption measurements were made using a previously described regeneratively amplified titanium:sapphire laser system operating at a 1 kHz repetition rate outfitted with a CCD array detector (Ocean Optics PC2000) for simultaneous collection of spectral and kinetic data.<sup>23,24</sup> All samples were filtered through a 0.45  $\mu\text{m}$  PTFE filter before measurement in a 2 mm quartz cuvette. The frequency-doubled output from the laser provides 400 nm, 80 fs pulses to drive an OPA, which generates the excitation light at 550 nm. Focusing a few microjoules of the 800 nm fundamental into a 1 mm  $\text{CaF}_2$  disk generated a white light continuum probe pulse. The  $\text{CaF}_2$  disk was translated to prevent damage to the disk. All-reflective optics were used to focus the 800 nm pulse into the  $\text{CaF}_2$  and recollimate the white light output, thus limiting the chirp on the white light pulse to  $<200$  fs from 450 to 800 nm. Cuvettes with a 2 mm path length were used, and the samples were irradiated with 0.5–1.0  $\mu\text{J}$ /pulse focused to a 200  $\mu\text{m}$  spot. The optical density at  $\lambda_{\text{max}}$  was typically 0.8 ( $\sim 10^{-4}$  M). The total instrument response function (IRF) for the pump–probe experiments was 130 fs. Kinetic analyses were performed at several wavelengths using a nonlinear least-squares fit to a general sum of exponentials using the Levenberg–Marquardt algorithm, while accounting for the presence of the finite instrument response. Fluorescence lifetime measurements were made using a Hamamatsu C4780 picosecond fluorescence lifetime measurement system, consisting of a C4334 Streakscope and a C4792-01 synchronous delay generator. The excitation light source was supplied by a home-built cavity-dumped Ti:sapphire laser<sup>25</sup> with a NEOS N13389 3 mm fused-silica acoustooptic modulator (AOM). The AOM was

driven by an NEOS Technologies N64389-SYN 10 W driver to deliver 38 nJ, sub-50 fs pulses at an 820 kHz repetition rate. The laser pulses were frequency doubled to 400 nm by focusing the 800 nm fundamental into a 1 mm type I BBO crystal. The energy of the resulting blue pulses was attenuated to approximately 1.0 nJ/pulse for all fluorescence lifetime experiments. The total IRF of the streak camera system was 25 ps. The samples were prepared in glass cuvettes, and the optical density at the excitation wavelength was typically 0.020–0.035. At  $\lambda_{\text{max}}$  of the samples, the optical density was typically 0.080–0.105. All fluorescence data were acquired in single-photon-counting mode using the Hamamatsu HPD-TA software. The data were fit using the Hamamatsu fitting module and deconvoluted using the laser pulse profile.

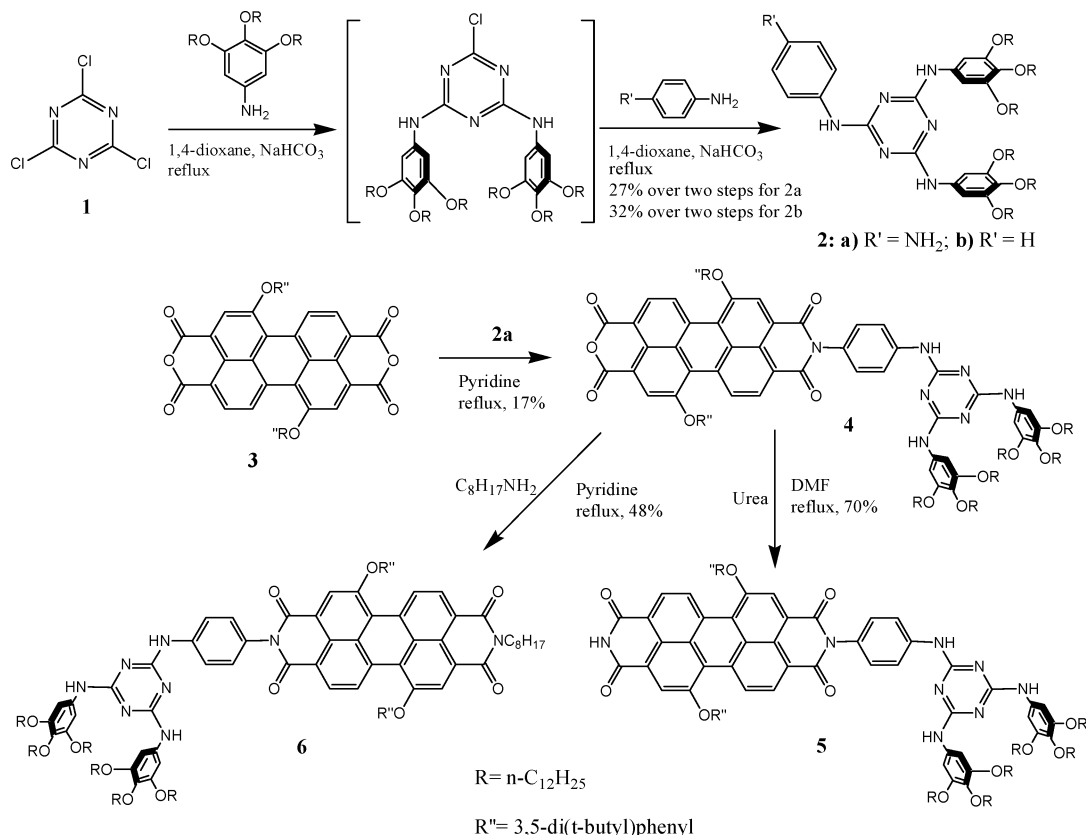
**X-ray Scattering Measurements.** X-ray scattering measurements were carried out using the undulator beam line 12-ID at the Advanced Photon Source (APS), Argonne National Laboratory. The X-ray scattering instrument utilized a double-crystal Si(111) monochromator<sup>26</sup> and a two-dimensional MARCCD detector. The X-ray wavelength was set at  $\lambda = 0.62$  Å, and the sample to detector distance was adjusted to achieve scattering across  $0.01 \text{ Å}^{-1} < q < 1.0 \text{ Å}^{-1}$ , where  $q = (4\pi/\lambda) \sin \theta$  ( $\lambda$  is the X-ray wavelength, and  $2\theta$  is the scattering angle). Glass capillary tubes (2.0 mm diameter) were used as sample containers. All the samples were filtered through 200 nm PTFE filters (Whatman) prior to the measurement. No significant differences in the data were observed within a range of concentrations between  $10^{-4}$  and  $10^{-3}$  M. Three measurements were made for each sample, and the average intensity was calculated. Solvent scattering was systematically measured and subtracted from the sample spectrum as a background.

**X-ray Scattering Analyses.** In the low-resolution scattering region below  $q = 0.1 \text{ Å}^{-1}$ , scattering follows the Guinier relationship,  $I(q) = I(0) \exp(-q^2 R_g^2/3)$ , parametrized in terms of the forward scattering amplitude,  $I(0)$ , and the radius of gyration,  $R_g$ .<sup>27,28</sup> Coordinate-based simulation of X-ray scattering curves from model structures was performed using computational approaches described previously.<sup>29–32</sup> The coordinate models of the aggregates were energy-minimized structures generated using the MM+ force field calculations.<sup>33</sup> Atomic pair distance distribution functions (PDFs) for model structures were determined from scattering patterns using indirect Fourier transform methods, which is the same approach used for the experimental data.<sup>34</sup> This procedure allowed both model and experimental PDFs to be determined in identical fashion using the program GNOM.<sup>34,35</sup> The reconstruction of the aggregate shape was done with the program DAMMIN<sup>36</sup> using for the input a GNOM “out” file containing experimental data. To obtain a more reliable solution, several independent DAMMIN runs were per-

- (20) Schmidt-Mende, L.; Fechtenkotter, A.; Müllen, K.; Moons, E.; Friend, R. H.; MacKenzie, J. D. *Science* **2001**, 293, 1119–1122.
- (21) Kim, J. Y.; Bard, A. J. *Chem. Phys. Lett.* **2004**, 383, 11–15.
- (22) Würthner, F.; Chen, Z.; Hoeben, F. J. M.; Osswald, P.; You, C.-C.; Jonkheijm, P.; Herrikhuysen, J. v.; Schenning, A. P. H. J.; van der Schoot, P. P. A. M.; Meijer, E. W.; Beckers, E. H. A.; Meskers, S. C. J.; Janssen, R. A. J. *J. Am. Chem. Soc.* **2004**, 126, 10611–10618.
- (23) Giaimo, J. M.; Gusev, A. V.; Wasielewski, M. R. *J. Am. Chem. Soc.* **2002**, 124, 8530–8531.
- (24) Rybtchinski, B.; Sinks, L. E.; Wasielewski, M. R. *J. Phys. Chem. A* **2004**, 108, 7497–7505.

- (25) Pshenichnikov, M. S.; de Boeij, W. P.; Wiersma, D. A. *Opt. Lett.* **1994**, 19, 572–574.
- (26) Seifert, S.; Winans, R. E.; Tiede, D. M.; Thiyagarajan, P. J. *Appl. Crystallogr.* **2000**, 27, 782–784.
- (27) Guinier, A.; Fournet, G. *Small Angle Scattering*; Wiley: New York, 1955.
- (28) Svergun, D. I.; Koch, M. H. *Rep. Prog. Phys.* **2003**, 66, 1735–1782.
- (29) Zhang, R.; Thiyagarajan, P.; Tiede, D. M. *J. Appl. Crystallogr.* **2000**, 33, 565–568.
- (30) Tiede, D. M.; Zhang, R.; Chen, L. X.; Yu, L.; Lindsey, J. S. *J. Am. Chem. Soc.* **2004**, 126, 14054–14062.
- (31) Ahrens, M. J.; Sinks, L. E.; Rybtchinski, B.; Liu, W.; Jones, B. A.; Giaimo, J. M.; Gusev, A. V.; Goshe, A. J.; Tiede, D. M.; Wasielewski, M. R. *J. Am. Chem. Soc.* **2004**, 126, 8284–8294.
- (32) Li, X.; Sinks, L. E.; Rybtchinski, B.; Wasielewski, M. R. *J. Am. Chem. Soc.* **2004**, 126, 10810–10811.
- (33) HyperChem, Hypercube, Inc., 1115 NW 1114th St., Gainesville, FL 32601.
- (34) Svergun, D. I. *J. Appl. Crystallogr.* **1992**, 25, 495–503.
- (35) Svergun, D. I.; Semenyuk, A. V.; Feigin, L. A. *Acta Crystallogr., A* **1988**, 44, 244–251.
- (36) Svergun, D. I. *Biophys. J.* **1999**, 76, 2879–2886.

Scheme 1. Synthesis of Compounds 5 and 6



formed, and the resulting solutions were averaged using the DAMAVER program package.<sup>37</sup>

**X-ray Diffraction (XRD).** Solid films were made by slow evaporation of a  $1 \times 10^{-4}$  M solution of **5** in methylcyclohexane (MCH) on a HMDS-treated silicon(100) substrate. Prior to film deposition the silicon substrate was prepared as follows. The substrates were subjected to three washings (acetone, methanol, and 2-propanol) and then dried with a stream of N<sub>2</sub>(g). The silicon was then methylated by exposure to 1,1,1,3,3,3-hexamethyldisilazane (HMDS) vapor for 12 h, followed by the same cleaning procedure as before. A Rigaku DMAX-A diffractometer using Ni-filtered Cu K $\alpha$  radiation was used for  $\theta$ -2 $\theta$  scans at the middle angles. At smaller angles,  $\theta$ -2 $\theta$  scans were performed on a Rigaku ATXG. The reflections from the film were referenced to the Si(400) reflection ( $2\theta = 69.2^\circ$ ) of the substrates.

**Scanning Electron Microscopy (SEM).** SEM samples were prepared via the same film growth procedure as for XRD. Prior to imaging, the sample was coated with 3 nm of Au via sputter coating. The instrument used was a Hitachi S4500 FE microscope.

**Transmission Electron Microscopy (TEM).** TEM observations were conducted using a Hitachi H8100 (200 kV) electron microscope. The TEM grid used upon which thin films were deposited was a copper grid covered with a thin carbon film (Ted Pella, Inc.).

## Results and Discussion

**Design and Synthesis.** We designed compound **5**, Scheme 1, to self-assemble using the synergistic effects of  $\pi$ - $\pi$  stacking, microsegregation, and hydrogen bonding. The use of several such interactions is commonly used to self-

assemble stable supramolecular structures.<sup>10–12,38</sup> The strong tendency of PDI to  $\pi$ - $\pi$  stack frequently results in aggregation.<sup>24,31,39,40</sup> Microsegregation is a complex phenomenon that arises from dispersion, solvophobic, and other weak interactions. We use a trialkoxybenzene moiety with long alkyl chains to introduce microsegregation into our PDI structures.<sup>41–44</sup> Microsegregation is enhanced if the molecule has both rigid and flexible parts,<sup>43</sup> as in **5** and **6**, where the nonpolar chains are flexible and the perylene core is rigid, and has been used to produce PDI-based liquid crystals.<sup>13,17,45,46</sup> The additional noncovalent interaction we introduce into our system is hydrogen bonding, via a melamine moiety and the unsubstituted imide group in PDI. This type of hydrogen-bonding receptor pair is known to form linear tapes or cylindrical tubes.<sup>12</sup>

To prepare compounds based on the principles outlined above, the syntheses presented in Scheme 1 were performed. Detailed procedures and characterization can be found in the Supporting Information. Briefly, the synthesis of **5** starts with

- (38) Schenning, A. P. H. J.; Herrikhuysen, J. v.; Jonkheijm, P.; Chen, Z.; Würthner, F.; Meijer, E. W. *J. Am. Chem. Soc.* **2002**, *124*, 10252–10253.
- (39) van der Boom, T.; Hayes, R. T.; Zhao, Y.; Bushard, P. J.; Weiss, E. A.; Wasielewski, M. R. *J. Am. Chem. Soc.* **2002**, *124*, 9582–9590.
- (40) Wang, W.; Han, J. J.; Wang, L. Q.; Li, L. S.; Shaw, W. J.; Li, A. D. Q. *Nano Lett.* **2003**, *3*, 455–458.
- (41) Kanie, K.; Yasuda, T.; Nishii, M.; Ujiie, S.; Kato, T. *Chem. Lett.* **2001**, 480–481.
- (42) Cheng, X. H.; Diele, S.; Tschierske, C. *Angew. Chem., Int. Ed.* **2000**, *39*, 592–595.
- (43) Tschierske, C. *J. Mater. Chem.* **1998**, *8*, 1485–1508.
- (44) Zheng, H.; Swager, T. M. *J. Am. Chem. Soc.* **1994**, *116*, 761–762.
- (45) Würthner, F. *Chem. Commun.* **2004**, 1564–1579.
- (46) Fuller, M. J.; Sinks, L. E.; Rybtchinski, B.; Giaimo, J. M.; Li, X.; Wasielewski, M. R. *J. Phys. Chem. A* **2005**, *109*, 970–975.

(37) Volkov, V. V.; Svergun, D. I. *J. Appl. Crystallogr.* **2003**, *36*, 860–864.



*N,N'*-bis(3,4,5-tridodecyloxy)phenyl-*N''*-(4-aminophenyl)-melamine (**2a**) that was prepared by a one-pot reaction of 1,3,5-trichloro-2,4,6-triazine (**1**) with 2 equiv of 3,4,5-tridodecyloxyaniline<sup>47</sup> and 1,4-diaminobenzene. Model compound **2b** was prepared via an analogous method. The coupling of **2a** with 1,7-bis(3',5'-di-*tert*-butylphenoxy)perylene-3,4,9,10-tetracarboxydianhydride (**3**) was carried out in refluxing pyridine followed by treatment of the resulting monoanhydride with urea in refluxing DMF to yield **5**. A model compound, **6**, which has an alkyl chain, instead of hydrogen, on the nitrogen atom of one of the imide groups was designed to hinder the formation of hydrogen bonds. It was prepared by reacting *n*-octylamine with anhydride **4**.

**Self-Assembly of Nanostructures.** The UV-vis spectra of **5** and **6** in THF at  $10^{-4}$  M show two maxima, Figure 1A, which correspond to the  $0 \rightarrow 0$  (537 nm) and the  $0 \rightarrow 1$  (503 nm) transitions, and are typical of monomeric PDI.<sup>31</sup> The spectra of **5** and **6** in THF at much lower concentrations ( $1.5 \times 10^{-6}$  M, not shown) are essentially unchanged. By contrast, in MCH at  $10^{-4}$  M the relative intensities of the  $0 \rightarrow 0$  and  $0 \rightarrow 1$  transitions for both **5** and **6** are reversed, Figure 1B, which indicates that the PDI molecules are aggregated in a cofacial (H-aggregate) geometry.<sup>39,45</sup> This concentration is within the range typically used for the small-angle X-ray scattering (SAXS) experiments described below. Decreasing the concentration of **5** and **6** in MCH to  $1.5 \times 10^{-6}$  M results in the reappearance of a spectrum for **6** that is characteristic of monomeric PDI, while that for **5** remains characteristic of cofacial aggregates, Figure 1C. Although these spectra are suggestive, they cannot distinguish between formation of a cofacial aggregate that does not involve hydrogen bonding and one that does. In the absence of any other interactions, such as cofacial  $\pi$ - $\pi$  stacking, a three-point hydrogen bond should readily form between the imide group of one molecule of **5** and the melamine of another molecule of **5** in MCH and not in THF.<sup>12,45</sup> We attempted to obtain further information regarding hydrogen bonding using  $^1\text{H}$  NMR by titrating a solution of **5** in MCH-*d*<sub>14</sub> with THF-*d*<sub>8</sub>. The  $^1\text{H}$  NMR spectra were severely broadened even when a 10-fold molar excess of THF was added to the MCH solution, precluding a clear separation of the effects of hydrogen bonding and aggregation upon oligomerization of **5** in MCH. Fortunately, we were able to determine the structure of this aggregate in solution directly using SAXS.

We have recently demonstrated that the X-ray scattering studies of monodisperse noncovalent systems using a synchrotron source is a powerful tool for the elucidation of solution-phase structures.<sup>29–32,48</sup> The ability to carry out structural studies of supramolecular assemblies at concentrations typical of photophysical measurements provides an important connection relating structure to observed function. SAXS measurements were used to determine structural features of oligomers of **5** in MCH solution ( $10^{-4}$ – $10^{-3}$  M) as described in the Experimental Section. Compound **5** shows an essentially linear Guinier plot, Figure 2, in the range  $0.002$

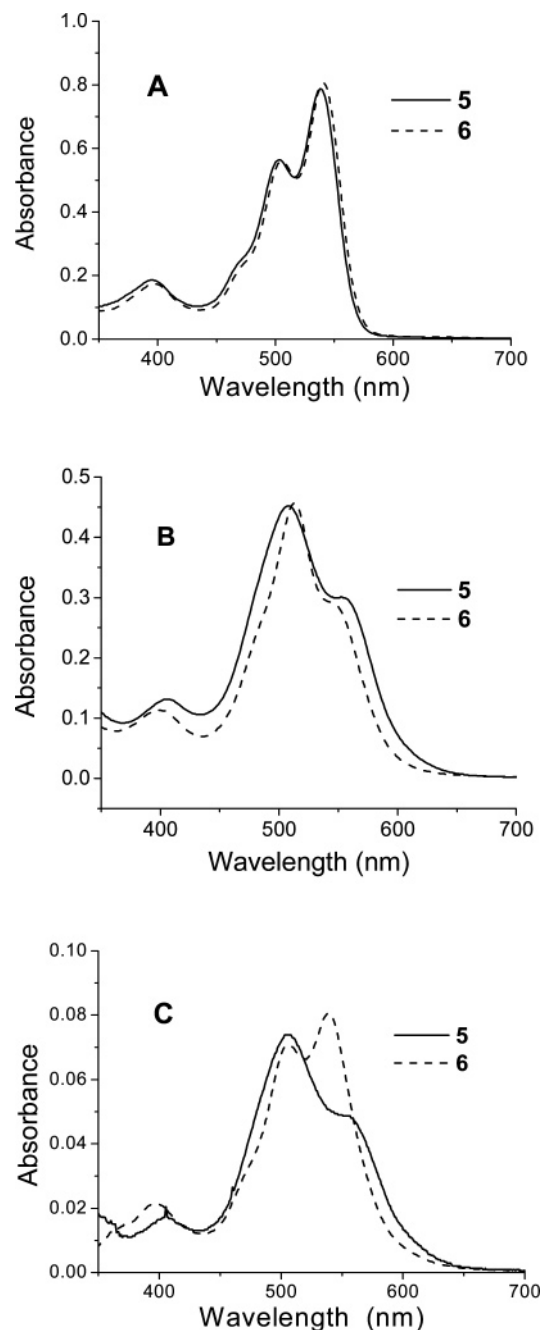


**Figure 1.** Comparisons of the UV-vis absorption spectra of **5** and **6** in (A) THF (each  $10^{-4}$  M, 2 mm path length cuvette), (B) MCH (each  $10^{-4}$  M, 2 mm path length cuvette), and (C) MCH (each  $1.5 \times 10^{-6}$  M, 1 cm path length cuvette).

$\text{\AA}^{-2} < q^2 < 0.08 \text{\AA}^{-2}$ , and a deviation from linearity in the region  $q^2 > 0.08 \text{\AA}^{-2}$ . This indicates that the aggregates of **5** are largely monodisperse.<sup>27,28</sup> A small degree of polydispersity is indicated by the upward deviation at higher  $q^2$ .  $R_g$  is not directly related to the molecular structure, but is the electron-density-contrast-weighted sum of the squares of the atomic distances from the center of mass, and hence depends on a combination of factors including electron density contrast with the solvent and the structure of the solvent-excluded and solvent-associated layers.<sup>27,28</sup> Thus, an  $R_g$  of  $26.0 \pm 0.1 \text{\AA}$  for **5** suggests that it forms relatively small aggregates in MCH solution.

The largely monodisperse character of **5** allows further analysis of the X-ray scattering data using atomic PDFs and

(47) Würthner, F.; Yao, S.; Heise, B.; Tschierske, C. *Chem. Commun.* **2001**, 2260–2261.

(48) Rybtchinski, B.; Sinks, L. E.; Wasielewski, M. R. *J. Am. Chem. Soc.* **2004**, *126*, 12268–12269.

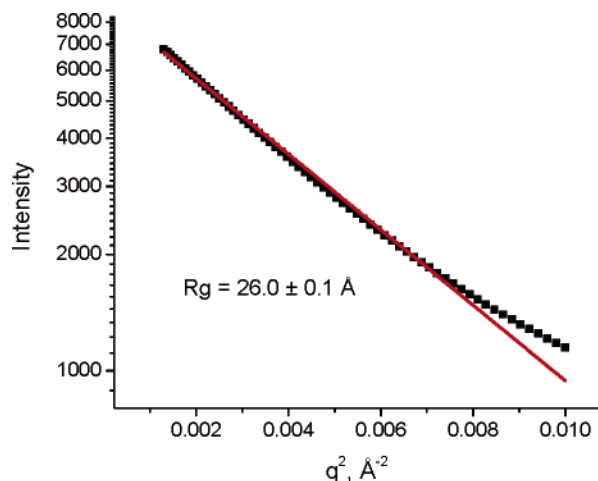


**Figure 2.** Guinier fit (line) for compound **5** in MCH (scatter, experimental data).

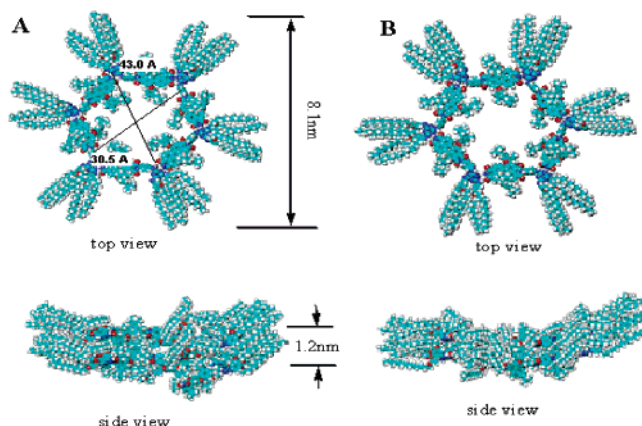


**Figure 3.** MM+-calculated model of the (A) helical structure or (B) stacked two-ring structure (the diameter is 8.1 nm, and the thickness of the two stacked PDI molecules is 1.2 nm). Inner diameters from PDI to PDI are shown in angstroms.

a simulated annealing procedure (see below). A direct comparison between the reciprocal-space scattering pattern and real-space molecular models can be made through a comparison of the PDFs. Scattering patterns are the rotationally averaged interference produced by collective intramolecular atomic scattering, and are related to the atomic PDF by a Fourier transformation.<sup>28</sup> Energy-minimized model structures were generated using the MM+ force field within HyperChem (Hypercube).<sup>33</sup> Two principal model structures, Figure 3, were found to give a good fit to the experimental data, Figure 4. Both structures show a cyclic motif consistent with hydrogen bonding between the individual PDI molecules. The first structure, Figure 3A, is a helical arrangement of twelve monomer units, while the second structure, Figure 3B, features two hexameric closed rings stacked on top of one another. Other models, such as pentagons and various linear structures, gave poorer PDF fits (see the Supporting Information), so the two dodecamers are the most probable structures. Figure 4 shows PDF patterns calculated from the atomic coordinates of energy-minimized models together with the PDF calculated from the experimental SAXS data using the program GNOM.<sup>34,49</sup> Unfortunately, PDF analysis

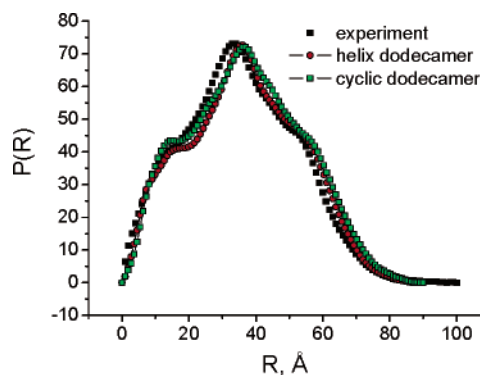


**Figure 4.** Atomic PDF of the models and the experiment results.

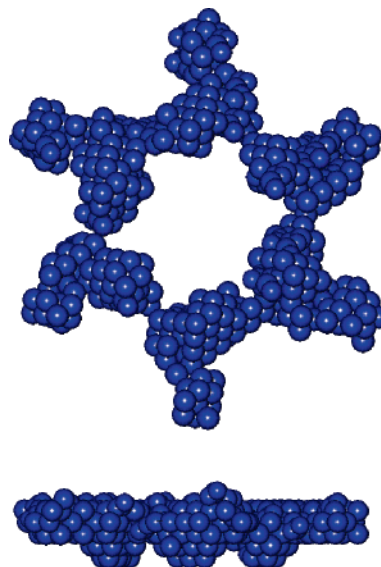


**Figure 5.** Reconstructed aggregate by simulated annealing (top, top view; bottom, side view).

does not allow us to distinguish between two stacked cyclic hexamers and a dodecameric helix. An analysis of the radii of gyration of the models also proves inconclusive, as both models have  $R_g \approx 26$  Å.

To corroborate the PDF analysis, an ab initio reconstruction of the aggregate shape from the experimental scattering data was performed using the simulated annealing procedure utilized in the program DAMMIN.<sup>36</sup> To achieve stable solutions and to obtain the most probable model, the independent models from several DAMMIN runs were superimposed and averaged using the program DAMAVER.<sup>37</sup> First, the reconstruction was run starting from a spherical particle with no symmetry. This resulted in an averaged structure with dimensions  $75 \times 55 \times 15$  Å. Then the reconstruction was run introducing 6-fold symmetry and a cylindrical geometry, which is consistent with the 6-fold symmetry of the aggregates suggested by the PDF analysis. The resulting averaged structure, Figure 5, has an outer diameter of 78 Å and an inner diameter of about 28 Å, is 10 Å thick, and closely matches the energy-minimized models in Figure 3. Simulated annealing reconstruction indicates that structures significantly larger or smaller than two stacked cyclic hexamers or a helical dodecamer most probably do not form. Thus, a single cyclic PDI hexamer resulting from hydrogen bonding can be ruled out since its thickness would

(49) Petoukhov, M. V.; Eady, N. A. J.; Brown, K. A.; Svergun, D. I. *Biophys. J.* **2002**, *83*, 3113–3125.

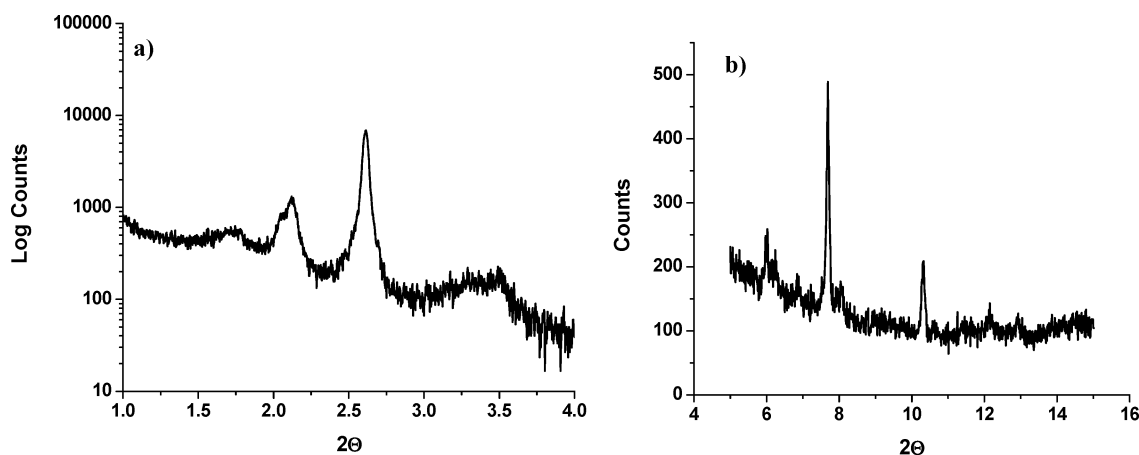


**Figure 6.** Scans ( $\theta$ – $2\theta$ ) of the assembly deposited out of MCH onto HMDS-treated Si(100), revealing  $d$  spacings of (a) 41.55 Å ( $2\theta = 2.124^\circ$ ) and 33.78 Å ( $2\theta = 2.612^\circ$ ) and (b) 11.20 Å ( $2\theta = 7.89^\circ$ ) and 8.41 Å ( $2\theta = 10.51^\circ$ ). Note the less intense peaks indicative of another, less prevalent, packing phase.

be significantly smaller than that observed in the reconstructed aggregate. Moreover, since no aromatic  $\pi$ – $\pi$  stacking occurs in a single cyclic hexamer, its UV–vis spectrum would not demonstrate the spectral shift typical of stacking that is observed for MCH solutions of **5**, Figure 1. Aggregates larger than dodecamers, e.g., three-turn helices or a stack of three cyclic hexamers, would result in thicker structures incompatible with the simulated annealing reconstruction as well. We have previously observed preferential dimer formation for large covalent arrays containing several PDI molecules under similar conditions, so the formation of cofacially stacked dimers appears to be a particularly stable structure.<sup>24,31,48</sup>

Solutions in MCH of the supramolecular assembly were deposited onto various substrates, and the resulting solids were characterized by XRD, TEM, and SEM. X-ray diffraction  $\theta$ – $2\theta$  scans at medium and wide angles reveal  $d$  spacings of 41.55, 33.78, 11.20, and 8.41 Å, Figure 6. The 41.55 and 33.78 Å spacings correlate well with the inner and outer diameters, respectively, of the central PDI cyclic structure as labeled in Figure 3. The 11.20 Å spacing correlates with the overall thickness of the stacked dimer of cyclic hexamers or the helical dodecameric structures, Figure 3, while the 8.41 Å spacing cannot be readily assigned to any obvious distance determined for the solution structure. The close correspondence between the XRD data in the solid film with those of SAXS in solution suggests that the solution-phase structural motif is largely retained in the solid state. Other reflections, presumably due to alternate packing phases, are present, but much weaker than the reflections mentioned above. TEM imaging, Figure 7, reveals well-defined structures with sharp edges ranging from 60 down to 10 nm in diameter, which is approximately the diameter of a single hexameric ring, as elucidated by SAXS. The presence of the wider structures suggests that the single ~10 nm diameter cylindrical nanostructures associate further to form bundles. SEM images from the samples used for solid-state XRD reveal structures with a cylindrical shape as well, Figure S3 in the Supporting Information. Attempts to obtain additional detail on these structures using both atomic force and scanning tunneling microscopies were unsuccessful, due largely to poor lateral resolution using the former technique and low conductivity using the latter technique.

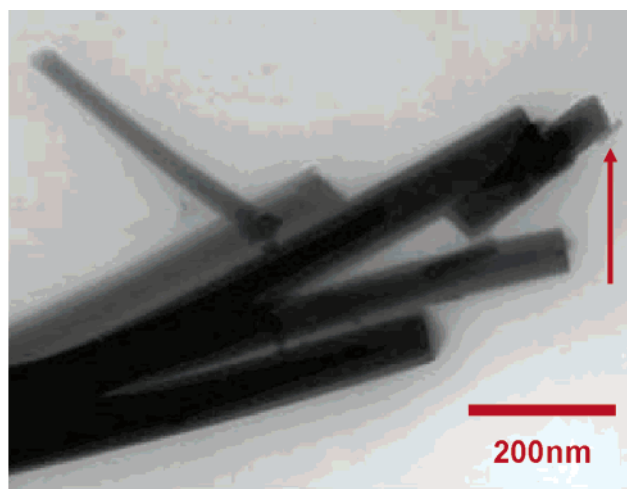


**Figure 7.** TEM image of the bundled cylindrical nanostructures comprised of **5** in the solid state. The smallest diameter column indicated by the arrow has a diameter of about 10 nm.

**Photophysics and Electron Transfer.** The presence of the tridodecyloxybenzene (TDB) moiety in **5** introduces the possibility that intramolecular photoinduced electron transfer may occur following photoexcitation of the PDI chromophore. The hydrogen-bonded structure of oligomeric **5** affords two different potential through-bond electron-transfer pathways: through hydrogen bonds between monomers (labeled HB) and through covalent bonds within a single monomer (labeled CB), Figure 8. Importantly, the distance between TDB and PDI is much shorter through path HB than through path CB. Given the relatively long through-space distances between TDB and PDI, it is not likely that direct through-space electron transfer will contribute significantly to the overall electron-transfer rate. The photophysics of model compound **6** was studied and compared to that of monomeric **5** to aid in the elucidation of the photophysics of the dodecamer of **5**. Compound **6** cannot form oligomers using hydrogen bonds; thus, intramolecular electron transfer from TDB to PDI most likely occurs by pathway CB.

The one-electron oxidation potential of model compound **2b** measured by cyclic voltammetry is  $E_{\text{OX}} = 1.02$  V vs SCE in dichloromethane, which is very similar to that measured for TDB itself (1.1 V vs SCE).<sup>46</sup> The PDI one-electron

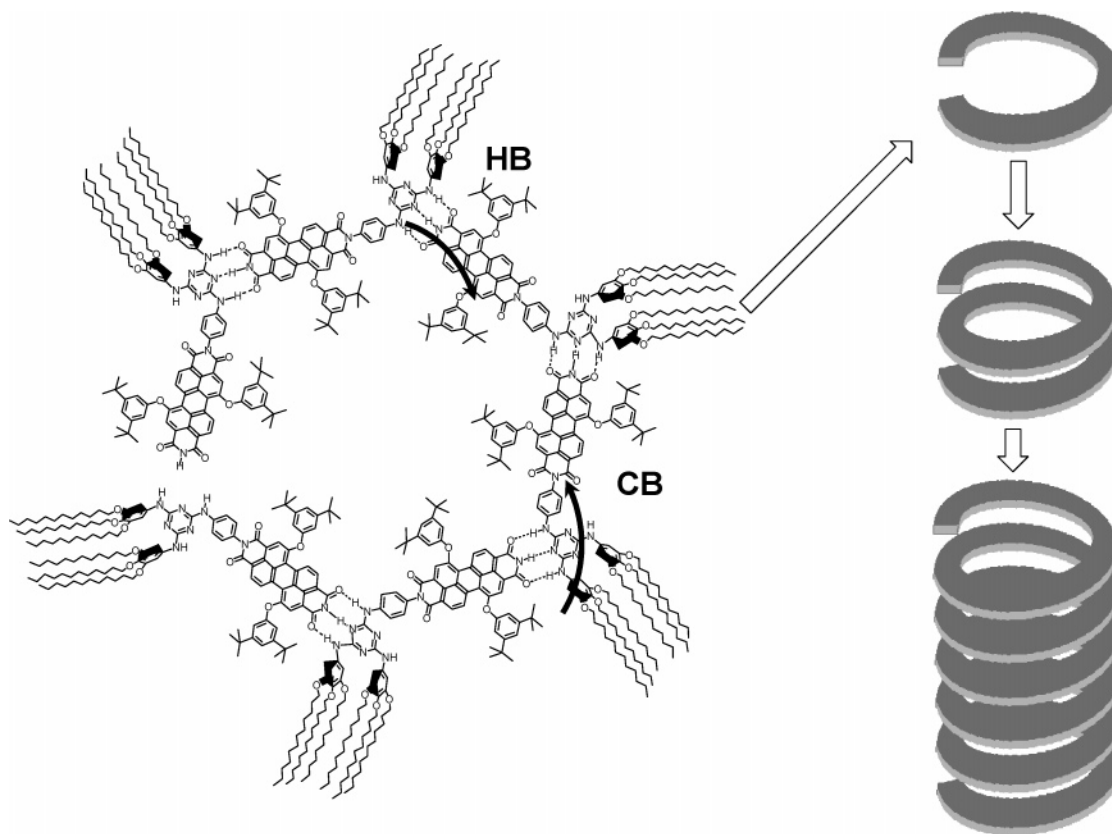


**Figure 8.** Proposed aggregation process for **5** in solution and in the solid state. The right side of this figure depicts formation of the two-turn helix structure followed by formation of an extended helix. The SAXS data support formation of either the two-turn helix or a pair of stacked rings (see Figures 3–5). The through hydrogen bond (HB) and through covalent bond (CB) electron-transfer pathways are indicated.

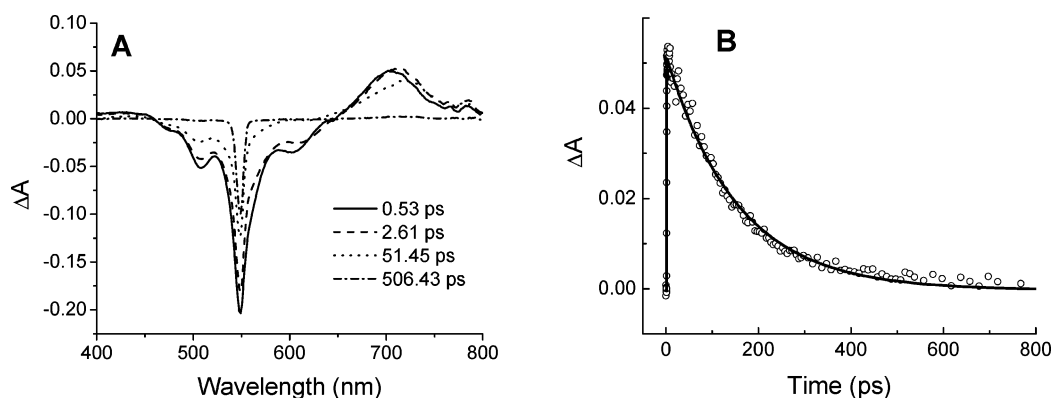


**Figure 9.** (A) Transient spectra of **6** in THF following a 550 nm, 80 fs laser flash. The sharp feature at 550 nm is residual scattered laser light. (B) Transient kinetics of **6** in THF obtained at 723 nm.

reduction potential is  $E_{\text{RED}} = -0.53$  V,<sup>39</sup> and its first excited singlet-state energy is  $E_S = 2.25$  eV.<sup>24</sup> The free energy of reaction for photoinduced electron transfer from TDB to PDI is  $\Delta G = E_{\text{OX}} = E_{\text{RED}} - E_S - e_o^2/r\epsilon_s + S$ , where  $e_o$  is the electronic charge,  $r$  is the distance between the ions (12 and 8 Å for the CB and HB pathways, respectively),  $\epsilon_s$  is the static dielectric constant of the medium ( $\epsilon_s = 6.9$  for THF and 2.0 for MCH), and  $S$  is the difference between the energies of the ion pair product in the polar solvent in which  $E_{\text{OX}}$  and  $E_{\text{RED}}$  are measured and other less polar solvents in which the electron-transfer rate constants are measured. The value of  $\Delta G$  for the reaction  $\text{TDB} - 1^* \text{PDI} \rightarrow \text{TDB}^{\bullet-} - \text{PDI}^{\bullet+}$  in polar solvents wherein  $e_o^2/r\epsilon_s \cong S \cong 0$ , is  $-0.7$  eV. The value of  $\Delta G$  should be substantially more positive in less

polar MCH, although accurate estimates of  $S$  using the Weller formalism are difficult in very nonpolar solvents.<sup>50,51</sup>

The transient absorption spectra of model compound **6** in THF are shown in Figure 9A. The spectra show a small bleach at 600 nm, which is due to stimulated emission from PDI.<sup>52</sup> The time constant of the recovery of this bleach,  $\tau_{\text{CS}} = 17 \pm 4$  ps, corresponds to deactivation of the lowest excited singlet state of PDI by charge separation and matches the decay of the excited-state absorption at 705 nm. The PDI

(50) Weller, A. *Z. Phys. Chem.* **1982**, *133*, 93.

(51) Greenfield, S. R.; Svec, W. B.; Gosztola, D.; Wasielewski, M. R. *J. Am. Chem. Soc.* **1996**, *118*, 6767.

(52) Weiss, E. A.; Ahrens, M. J.; Sinks, L. E.; Gusev, A. V.; Ratner, M. A.; Wasielewski, M. R. *J. Am. Chem. Soc.* **2004**, *126*, 5577–5584.



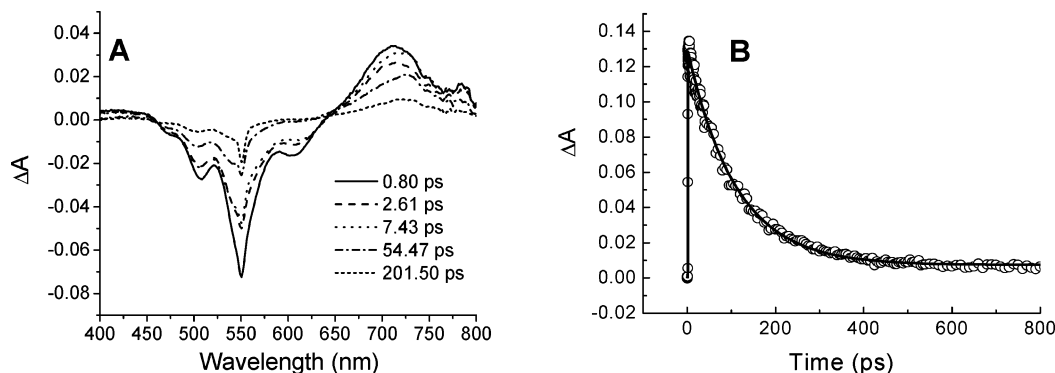


**Figure 10.** (A) Transient spectra of **5** in THF following a 550 nm, 80 fs laser flash. The sharp feature at 550 nm is residual scattered laser light. (B) Kinetics of **5** in THF at 723 nm.

radical anion band observed at 723 nm monitors the formation of the ion pair.<sup>24,39</sup> The time constant for charge separation is the same as that for the decay of  $^1\text{PDI}$  monitored by the disappearance of the stimulated emission bleach ( $\tau_{\text{CS}} = 17$  ps). The recombination of the ion pair is represented by the decay of  $\text{PDI}^{\bullet-}$  at 723 nm, with  $\tau_{\text{CR}} = 106 \pm 4$  ps, Figure 9B. These dynamics correspond to electron transfer through the intramolecular covalent path CB, the only path available in **6**.

The interactions between monomers of **5** that promote their self-assembly into the dodecamers are disrupted in polar solvents such as THF, Figure 1. Thus, THF provides an environment to study the photophysics that arise from monomeric **5**. Its transient spectra, Figure 10A, are almost identical to those of model compound **6**. Fits to the rise and decay kinetics of  $\text{PDI}^{\bullet-}$  monitored at 710 nm demonstrate that intramolecular charge separation and recombination are  $\tau_{\text{CS}} = 15 \pm 2$  ps and  $\tau_{\text{CR}} = 110 \pm 30$  ps, respectively, Figure 10B. Thus, the rates of photoinduced charge separation and recombination for monomeric **5** are almost identical to those of model compound **6**, as is expected from their similar structures.

In MCH **5** self-assembles to form the cyclic dodecameric aggregate in which hydrogen bonding provides another potential pathway (HB) for electron transfer. The UV-vis spectra of the PDI chromophores in  $\sim 10^{-4}$  M solutions of **5** and **6** in MCH display features commonly observed when PDIs form cofacial H-aggregates, Figure 1B.<sup>24,31,39</sup> However, at concentrations below  $10^{-5}$  M, the UV-vis spectrum of **5**, Figure 1C, indicates that the PDI molecules remain cofacially stacked, while the spectrum of **6** shows that it is disaggregated. Thus, the photophysics intrinsic to monomeric **6** in MCH must be obtained at low concentrations. These concentrations are too low for accurate transient absorption measurements, so time-resolved fluorescence spectroscopy is used to determine the deactivation pathways following photoexcitation of monomeric **6** in MCH.

Time-resolved fluorescence measurements of **6** at low concentrations show strong fluorescence emission having a spectrum characteristic of monomeric PDI, Figure 11. The spectrum decays with  $\tau_{\text{obs}} = 1.4$  ns, Figure 11 (inset), which is somewhat shorter than the 4.5 ns fluorescence lifetime of PDI with no electron donors attached.<sup>24</sup> If the lifetime shortening observed for **6** is due solely to electron transfer competing with the decay of the PDI lowest excited singlet

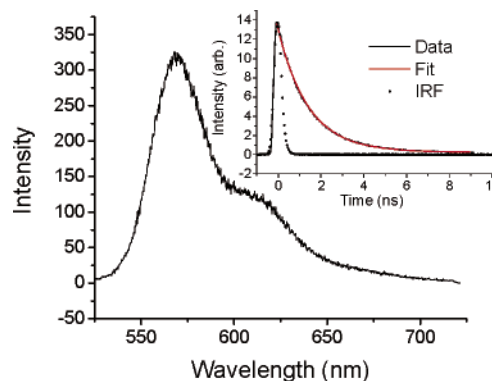


**Figure 11.** Emission spectrum of  $10^{-6}$  M **6** in MCH integrated between 1 and 6 ns following a 400 nm, 50 fs laser flash. Inset: fluorescence decay kinetics monitored at 570 nm.

state, then the time constant for electron transfer is  $1/\tau_{\text{ET}} = (1/\tau_{\text{obsd}}) - (1/\tau_0)$ , where  $\tau_{\text{obsd}}$  is the measured fluorescence lifetime and  $\tau_0$  is the fluorescence lifetime of PDI itself. Using this expression,  $\tau_{\text{ET}} = 2.0$  ns, which shows that intramolecular electron transfer from TDB to  $^1\text{PDI}$  in monomeric **6** in MCH is approximately 100-fold slower than the corresponding reaction in THF. This is consistent with the significantly more positive  $\Delta G$  for charge separation expected in MCH relative to THF. As the concentration of **6** is increased, aggregates form and the observed photophysics become more complex. Since **6** lacks the hydrogen-bonding receptor, the solution-phase structure of these aggregates is expected to be different from that of **5**. Unfortunately, their polydisperse nature precludes the use of SAXS to elucidate their structure in solution.

The transient absorption spectra of the dodecameric aggregate of **5** in MCH, Figure 12A, display a broad absorption in the red and a positive feature at 550 nm typical of singly reduced PDI dimers.<sup>24,39</sup> The 550 nm absorption appears with  $\tau_{\text{CS}} < 1$  ps, and then all bands recover to baseline with biexponential kinetics having a fast component of  $4.2 \pm 0.5$  ps (60%) and a slower component of  $164 \pm 45$  ps (40%). The transient absorption experiments were performed at four different temperatures (288, 293, 298, and 308 K), and the observed kinetics were invariant over this temperature range. The fact that the charge recombination rates are temperature independent supports the idea that the observed biexponential charge recombination is not due to two competing processes that equilibrate between 288 and 308 K, but rather is due to two distinct processes that are

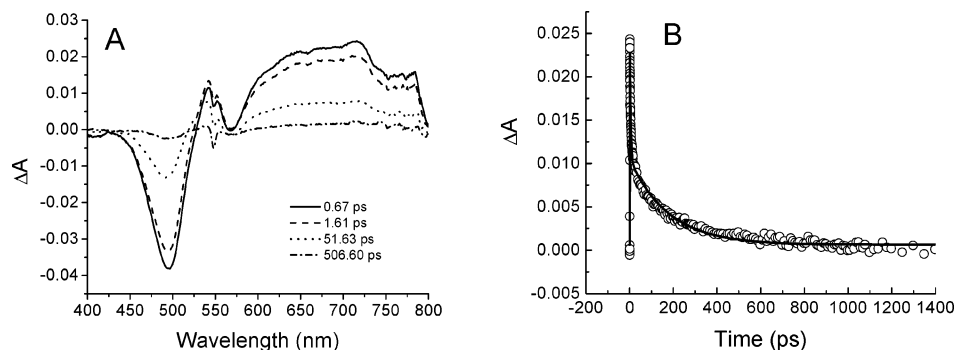


**Figure 12.** (A) Transient spectra of **5** in MCH at 298 K following a 550 nm, 80 fs laser flash. The sharp feature at 550 nm is residual scattered laser light. (B) Transient kinetics of **5** in MCH at 298 K obtained at 720 nm.

not kinetically connected, such as charge recombination from two different structures.

We have previously shown that in donor–acceptor systems based on cofacial PDI aggregates an excimer-like state is formed within the instrument response time.<sup>24</sup> In the case of **5** the formation of the excimer-like state is followed by ultrafast electron transfer to form  $\text{TDB}^{\bullet+}\text{--PDI}^{\bullet-}$ , as indicated by the observed spectral features associated with the radical anion in cofacial PDI dimers.<sup>24,39</sup> The electron transfer is assumed to occur through the fast HB pathway, as the observed electron-transfer rates are more than 2000 times faster than those seen in the monomeric model compound **6**. This is consistent with previous work on electron transfer through hydrogen bonds, wherein short donor–acceptor distances and strong coupling may explain very fast electron transfer.<sup>53</sup> We attribute the biexponential recovery of  $\text{TDB}^{\bullet+}\text{--PDI}^{\bullet-}$  to charge recombination in two different populations of PDI. If the structure of **5** in MCH is a helical dodecamer, the two terminal PDI molecules each form stacked dimers with an adjacent PDI. The structure and the solvent environment of these two dimers are certainly different from those of the remaining four pairs of stacked PDI molecules in the dodecamer. These differences most likely result in differences in both charge separation and recombination rates between the two populations. This is consistent with the observed amplitudes for the two components of the biexponential charge recombination, with about 60% of the population recombining in 4 ps, while about 40% recombines more slowly in 164 ps, Figure 12B. The charge separation is too fast (<1 ps) to cleanly resolve biexponential behavior for the corresponding charge separation process. For two cofacially stacked cyclic hexamers there is no single obvious structural feature that would lead to the observed biexponential behavior. Therefore, the photophysical data are best explained by the helical dodecamer model.

### Conclusions

We have demonstrated that large-diameter PDI cylindrical nanostructures can be constructed through self-assembly of

a suitably functionalized PDI monomer, and have characterized the structure of these aggregates in solution as well as in the solid state. The nanostructures in the solid state largely retain the structural pattern observed in the dodecameric aggregates present in solution. The photophysical properties of **5** and **6** in THF and MCH are very similar in THF and dramatically different in MCH. Since both **5** and **6** are monomeric in THF and possess the same covalently linked donor and acceptor, these compounds demonstrate similar rates of photoinduced charge separation and subsequent recombination. In MCH the dodecameric aggregate of **5** exhibits efficient ultrafast photoinduced charge separation in <1 ps, whereas charge separation in the monomeric model compound **6** is nearly 2000-fold slower. It is apparent that the hydrogen bonds linking the monomers of **5** into the dodecamer provide a shorter distance, through-bond pathway through which substantially faster electron transfer occurs. This pathway provides new photofunctionality in these self-assembled supramolecular structures that is not present in their constituent monomers. However, we cannot completely rule out additional contributions to the overall observed rate enhancement from favorable changes in energy of both the PDI excited state and radical ion pair state product due to  $\pi$ -stacking in the supramolecular structure.

**Acknowledgment.** Work performed at Northwestern University was supported by the Office of Naval Research (Grant N00014-05-1-0021) and DARPA (Grant HR0011-04-C0071). X-ray structure analysis at the Advanced Photon Source (A.J.G., X.Z., D.M.T.) was supported by the U.S. Department of Energy, Office of Science, Office of Basic Energy Sciences, under Contract No. W-31-109-ENG-38. Use of the SEM and the XRD facilities was supported by the NSF-MRSEC program through the Northwestern Materials Research Center (Grant DMR-0076097). We thank Mr. Wenhao Liu for performing the time-resolved fluorescence measurements of **6**. We thank Ms. Erin Chernick and Dr. Michael Ahrens for providing reference NMR spectra.

**Supporting Information Available:** Experimental details including synthesis, SAXS, and photophysical data. This material is available free of charge via the Internet at <http://pubs.acs.org>.

CM051461S

(53) de Rege, P. J. F.; Williams, S. A.; Therien, M. J. *Science* **1995**, 269, 1409–1413.